Wavefront control in space with MEMS deformable mirrors for exoplanet direct imaging

Kerri L. Cahoy
Anne D. Marinan
Benjamin Novak
Caitlin Kerr
Tam Nguyen
Matthew Webber
Grant Falkenburg
Andrew Barg

Wavefront control in space with MEMS deformable mirrors for exoplanet direct imaging

Kerri L. Cahoy
Massachusetts Institute of Technology
Department of Aeronautics and Astronautics
77 Massachusetts Avenue
Cambridge, Massachusetts 02139
  and
Massachusetts Institute of Technology
Department of Earth and Planetary Science
77 Massachusetts Avenue
Cambridge, Massachusetts 02139
E-mail: kcahoy@mit.edu

Anne D. Marinan
Benjamin Novak
Caitlin Kerr
Tam Nguyen
Massachusetts Institute of Technology
Department of Aeronautics and Astronautics
77 Massachusetts Avenue
Cambridge, Massachusetts 02139

Matthew Webber
Massachusetts Institute of Technology
Department of Earth and Planetary Science
77 Massachusetts Avenue
Cambridge, Massachusetts 02139

Grant Falkenburg
Andrew Barg
Massachusetts Institute of Technology
Department of Aeronautics and Astronautics
77 Massachusetts Avenue
Cambridge, Massachusetts 02139

Abstract. To meet the high contrast requirement of 1×10^{-10} to image an Earth-like planet around a sun-like star, space telescopes equipped with coronagraphs require wavefront control systems. Deformable mirrors (DMs) are a key element of a wavefront control system, as they correct for imperfections, thermal distortions, and diffraction that would otherwise corrupt the wavefront and ruin the contrast. The goal of the CubeSat DM technology demonstration mission is to test the ability of a microelectro-mechanical system (MEMS) DM to perform wavefront control on-orbit on a nanosatellite platform. We consider two approaches for an MEMS DM technology demonstration payload that will fit within the mass, power, and volume constraints of a CubeSat: (1) a Michelson interferometer and (2) a Shack-Hartmann wavefront sensor. We clarify the constraints on the payload based on the resources required for supporting CubeSat subsystems drawn from subsystems that we have developed for a different CubeSat flight project. We discuss results from payload laboratory prototypes and their utility in defining mission requirements. © *The Authors. Published by SPIE under a Creative Commons Attribution 3.0 Unported License. Distribution or reproduction of this work in whole or in part requires full attribution of the original publication, including its DOI.* [DOI: 10.1117/1.JMM.13.1.011105]

1 Introduction

Scientists anticipated the existence of other Earth-like planets in the universe well before the first discoveries of exoplanets by astronomers: pulsar planet $PSR1257 + 12$[1] and 51 Pegasi b.[2] An Earth-like planet is normally thought of as a rocky planet with radius of $1 - 2R_E$ (Earth radii), enough gravity to retain a substantial atmosphere, and located close enough to its parent star that liquid water could exist in a stable form on its surface. Implied in this definition is the ability of an Earth-like planet to support life.

This paper addresses the technology needed in order to directly image an Earth-like planet. Direct imaging of exoplanets is an example of a challenging new high contrast (1×10^{-10}), high-dynamic range observation that seeks to identify an Earth-like planet around another star in the local solar neighborhood by blocking the parent star's light, using wavefront control to manage the contrast, and measuring atmospheric absorption features in its reflected light spectrum.[3] An Earth-like planet may be detected using methods other than direct imaging. Indeed, radial velocity and transit photometry observations have already delivered several promising candidates (e.g., the planets around Gliese 581,[4] Kepler

22b,[5] Tau Ceti e and f[6]). However, we address the challenge of characterizing an Earth-like planet, i.e., observing how light from the parent star is reflected off of the Earth-like planet over a range of wavelengths.[7] Recent observations of exoplanet transit secondary eclipses have yielded phase offsets due to longitudinal thermal gradients and broad-band spectral measurements for extrasolar giant planets.[8–11] The goal of the direct imaging method is to obtain high-resolution reflected light spectra of Earth-like extrasolar planets. These reflected light spectra contain continuum trends and absorption features that will not only tell us about the scattering properties, temperature, and pressure of the planet's atmosphere, but also identify which gases are present and in what abundances (e.g., Refs. 12–19). Reflected light spectral information is a key to determine whether or not these Earth-like planets contain life.

1.1 Direct Imaging Approach

In order to observe the reflected light spectrum of an Earth-like exoplanet, the instrument used must first be able to resolve the planet from the star and, second, have some way of "blocking" the parent star's light such that it does

not saturate the detector so the reflected light from the orbiting exoplanet can be detected. The Rayleigh criterion of $\theta = 1.22\lambda/D$ describes the minimum angular separation between two monochromatic point sources that can be unambiguously resolved by a telescope with primary circular aperture of diameter D at the wavelength λ. This is the angular separation of the first null in each point source's Airy function. The Airy function, or point spread function, describes the diffraction that occurs when the light from the point source passes through the circular aperture. The Airy function is a first-order Bessel function of the first kind, J_1, and the number 1.22 is the first zero of J_1 divided by π. Angular resolution can be improved by increasing D or decreasing λ.

An instrument called a coronagraph, originally developed to study the solar corona, uses an optical element to achieve the "blocking" of the parent star's light well enough that reflected light from an orbiting exoplanet can be detected. The coronagraph optical element can be as simple as an amplitude mask (e.g., Refs. 20 and 3), or it can be more complex and use both amplitude and phase to remove or relocate the parent star's light.[21–23] The coronagraph design must also consider the effect of the point spread function of each point source and the way that diffraction redistributes the light from the parent star across the image. High-performance coronagraphs are needed to achieve contrast ratios on the order of 1×10^{-10} in order to detect an Earth-like planet around a sun-like star.

There are other proposed methods for obtaining spectra of Earth-like exoplanets. Some examples include "combined-light" spectra obtained from transit photometry observations (e.g., Ref. 24) using an "external occulter" instead of an internal coronagraph (e.g., Ref. 25), or using interferometry (e.g., Refs. 26 and 27). The transit photometry method takes advantage of the fact that at some point during a transit observation, the exoplanet travels behind its parent star. This is called a "secondary eclipse." When the planet is in secondary eclipse, the observation is only the spectrum of the parent star. This can be compared with "combined-light" spectra that are obtained when both the planet and the parent star are in view. Challenges with the combined-light approach involve being able to discern the contribution of the reflected light from the planet from the much larger signal of the parent star, as well as understanding the variability of the parent star. The "external occulter" approach takes the occulting element from an "internal" coronagraph and places it at a large distance from the telescope. This approach requires precise manufacturing of the "starshade" used as the external occulting element as well as precise control of the starshade position. Interferometers can also be used as a type of single internal coronagraph or employed across multiple spacecraft in a distributed approach.[10] In this paper, we focus on technologies that apply to the "internal coronagraph" direct imaging method.

The stated 1×10^{-10} contrast ratio can be straightforwardly calculated. The contrast ratio between an exoplanet and its star depends on many factors, including the physical properties of the planet and star, the system geometry, background sources, and the instrumentation used. A simple way of estimating the required contrast is to assume that the planet reflects its incident star light isotropically. Thus, its apparent brightness is constant over its illuminated surface, like a Lambertian surface. Then, the contrast can be expressed as:[28]

$$C(\alpha) = \frac{2}{3} A_g(\lambda) \left(\frac{R_p}{d}\right)^2 \left[\frac{\sin(\alpha) + (\pi - \alpha)\cos(\alpha)}{\pi}\right], \qquad (1)$$

where α is the planet phase angle, R_p is the planet radius in km, d is the planet-star separation in km, and A_g is the geometric albedo. The geometric albedo generally takes values between 0 and 1 for the fraction of monochromatic light the planet reflects toward the observer at full phase at wavelength λ, although it can be larger than 1 for anisotropic scattering atmospheres or surfaces. If one assumes that the planet is at quadrature, $\alpha = \pi/2$, and that the geometric albedo at the wavelength of interest is 0.5, then for a Jupiter analog ($1R_J$), the contrast at 0.8 AU is 3.8×10^{-8} and at 10 AU is 2.4×10^{-10}. For a Neptune analog ($1R_N$), the contrast at 0.8 AU is 4.5×10^{-9} and at 10 AU is 3×10^{-11}. For an Earth analog ($1R_E$) at 1 AU with $A_g = 0.3$, the contrast is 1.2×10^{-10} (Ref. 16). High contrast is more difficult to achieve closer to the star than further away, but the d^{-2} dependence also means that planets farther from the star will be fainter in reflected light.

1.2 Role of Deformable Mirrors in Exoplanet Direct Imaging Systems

Thus, in order to image an Earth-like planet, an exoplanet direct imaging system needs to achieve a contrast ratio of 1×10^{-10}. A high-performance coronagraph is designed to meet this requirement. Even with adaptive optics on a large ground-based telescope, it is currently not possible to overcome the effects from atmospheric turbulence to achieve the high contrast needed to obtain high-resolution spectra of an Earth-like exoplanet at visible wavelengths.[29,30] While a space telescope does not have to overcome the effects of atmospheric turbulence, it is usually at the expense of smaller aperture size (e.g., due to launch cost and launch vehicle limitations) and the performance of a space telescope will still suffer from optical imperfections, thermal distortions, and diffraction that will corrupt the wavefront, create speckles, and ruin the contrast. Active optical control is still needed to achieve the desired contrast on a space telescope.

Ground-based adaptive optics systems that compensate for atmospheric turbulence (which is typically characterized by Fried parameter r_0 and Greenwood frequency τ_0) are designed to perform at higher speeds and with larger strokes than that needed by wavefront control systems on space telescopes used for astronomical observations that do not need to compensate for atmospheric turbulence. On the ground, a two-mirror woofer-tweeter (coarse-fine) wavefront control approach is frequently used[31] where the woofer corrects slower, larger amplitude, lower-frequency components and the tweeter corrects faster, smaller amplitude, higher-frequency components. In this paper, our proposed deformable mirror (DM) demonstration mission focuses on developing a low cost, easy-access-to-space platform for validating technologies used for the tweeters: higher actuator count, lower stroke DMs.

The need for high actuator count DMs for an exoplanet direct imaging mission is driven by the angular separation from an on-axis star about which we can look for an exoplanet, as the DM must have the authority to compensate for speckles and aberrations over this region. If a DM only has a few actuators, it can only correct for low spatial frequencies that are close to on-axis in the image plane,

corresponding to larger-scale distortions in the pupil plane. To be able to correct for speckles and aberrations "farther out" around a star so that we can look for exoplanets in the region known as the habitable zone, it is necessary to have mirrors with more actuators and the corresponding control over higher spatial frequencies (further off-axis in the image plane) as shown in Fig. 1.

1.3 Space Telescopes for Direct Imaging

It is desirable to use a space telescope for Earth-like exoplanet observations (as opposed to observations of larger and brighter gas or ice giant exoplanets) because even for ground-based telescopes with high performance adaptive optics systems[32] and an ideal coronagraph, the speed of atmospheric turbulence and the limited number of photons from the exoplanet target, in addition to constraints on viewing geometry and integration time, limit the achievable contrast.[29,30] Observations that can capture features in the atmospheric spectra of an Earth-like exoplanet require wavefront control, because even a well-engineered space telescope with a sophisticated high-performance coronagraph[20,33] will have mid and high spatial frequency wavefront aberrations

that will degrade the achievable image contrast.[21,34,35] Drifts in the optic shapes over the long integration times necessary for such a scientific observation should be comparatively small and slow, thus wavefront control techniques can be used to reduce the phase errors to an acceptable level (e.g., <1 nm). Wavefront control systems are also needed to manage speckles that result from diffraction, phase errors, and noise. In co-operation with the spacecraft attitude determination and control system (ADCS), wavefront control systems can also be used to address submilliarcsecond pointing errors.[36] The spacecraft ADCS system is designed to provide "coarse pointing" which is on the order of the angular resolution of the system over periods of time that are shorter than twice the desired integration time. Examples of ADCS-induced disturbances include structural vibrations from reaction wheel imbalances during momentum management. Other than orbit and orientation contributions to thermal variation, the imaging detector may also be actively cooled to help reduce thermal noise (dark current), and the cyclic cryo-coolers used may also induce angular disturbances. In order to achieve the fine pointing requirements, the optical system design is as structurally isolated as possible, and fast

(a)

(b)

(c)

(d)
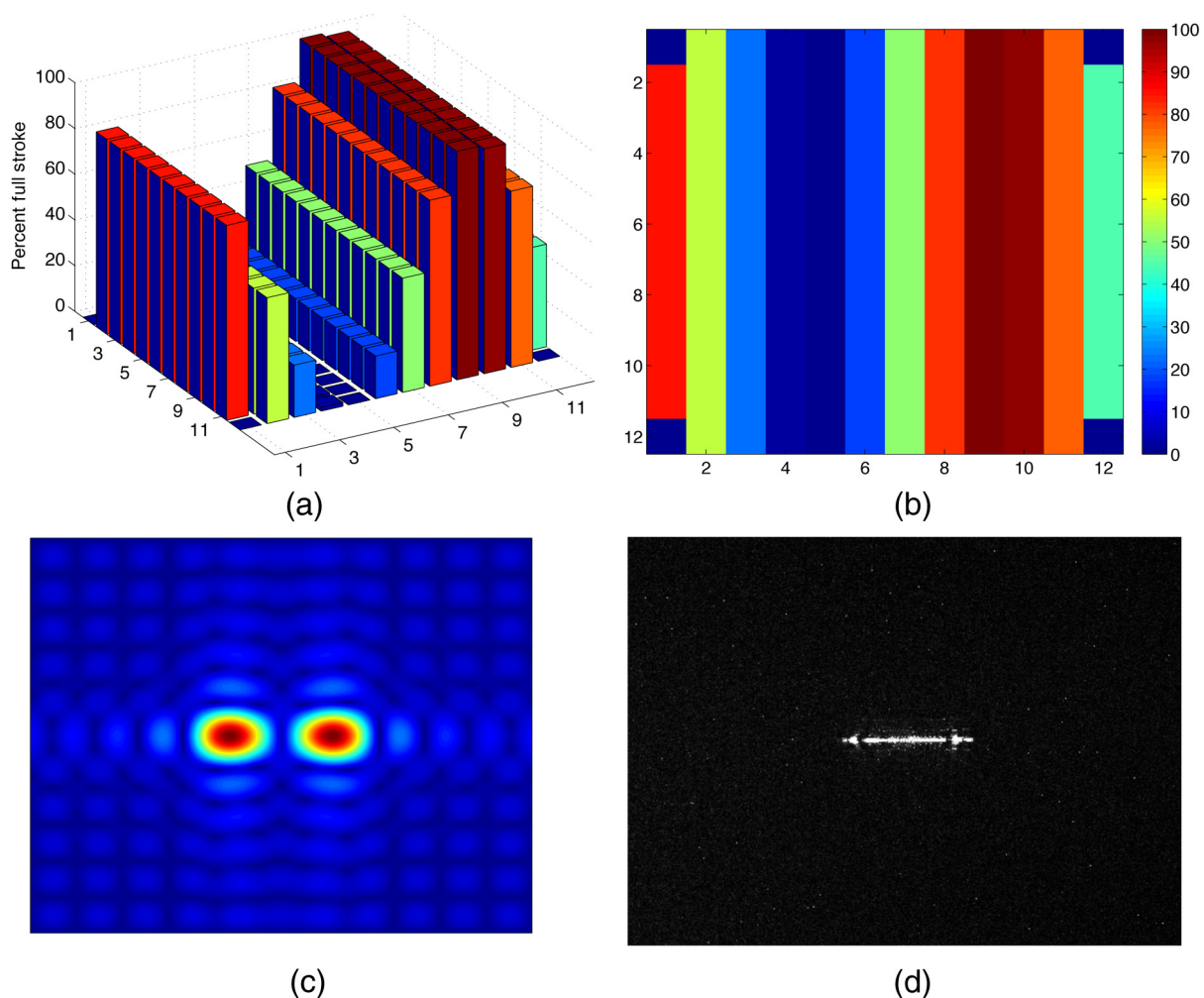
Fig. 1 Illustration of how number of actuators on the deformable mirror (DM) [simulating the Boston Micromachines Corporation (BMC) 144 actuator Multi] map to spatial frequency. (a) Commanding a cosine on the DM, $\cos(2\pi f_0 x)$ where $f_0 = 0.25$. (b) Top view of the commanded DM, with the four inactive corner actuators. (c) Two-dimensional fast Fourier transform (FFT) of the cosine DM showing peaks at the spatial frequency of 0.25. (d) Image taken using the BMC Multi commanded as shown in (a).

steering mirrors are typically used to reduce the impact of vibrations.

1.4 Goals of the CubeSat DM Demonstration

The development of a space telescope equipped with a high-performance coronagraph and DM wavefront control system that is capable of the 1×10^{-10} contrast needed to directly image Earth-like exoplanets is expected to be on the order of several hundreds of millions of dollars to over a billion dollars.[37] The goal of the CubeSat DM demonstration is to provide a low-cost way to quickly test small, low power, higher actuator-count DM in-orbit, such as those shown in Fig. 2, and raise their technology readiness level (TRL) for use on larger, more capable space telescopes. While several important environmental tests can be performed using these mirrors on the ground (thermal vacuum, vibration, life cycle testing, and to a limited extent radiation), it is important to demonstrate that simple wavefront control systems utilizing new DM technologies have stable, well calibrated, and predictable performance in orbit. This is particularly important to emphasize, as there is no opportunity to "tweak" or "adjust" a wavefront control system in orbit after launch. It is of particular importance to fully develop robust flight software to control these mirrors and systems, to incorporate them as sensors with spacecraft ADCS, estimators, and fine pointing algorithms, and to determine how best to capture performance and calibration data along with science observations and transmit it to the ground, as well as to monitor for degradation in performance over time and assess failures.

1.5 Context and Related Efforts

The most relevant recent effort was the Boston University PICTURE (Planet Imaging Concept Testbed Using a Rocket Experiment)[38] sounding rocket experiment, which flew with a Boston Micromachines microelectromechanical system (MEMS) DM for high contrast wavefront control in 2007. The rocket attitude control system provided 627 milli-arcseconds (mas) root mean square (RMS) body pointing and the fine pointing system successfully stabilized the telescope beam to 5.1 mas RMS using an angle tracker camera and fast steering mirror. However, due to a communications system malfunction all MEMS DM performance data were unfortunately lost. There will be a future repeat attempt at the PICTURE mission. Even so, however, the total sounding rocket observing time is on the order of 5 min (320 s) which is not sufficient to demonstrate the long term, accurate calibration, and operation of an MEMS DM over the multiple hours of integration necessary for building confidence in robust DM performance during hours of photon starved 10^{-10} contrast direct imaging of an Earth-like exoplanet, never mind repeat usage throughout a multiyear mission.

Another relevant effort was the South Korean MEMS Telescope for Extreme Lightning (MTEL) in 2009[39,40] which used a one-axis torsional spring tilt single actuator trigger mirror and a two-axis tip–tilt electrostatic comb drive 8×8 MEMS mirror array in an LEO orbit. However, the actuators in this mirror are very different from the high actuator count MEMS DMs needed for wavefront control for a high contrast imaging application. The MTEL trigger mirror operated in tilt only with two possible positions (on/off). The tip–tilt torsional spring array was for selective beam directing and not precise wavefront control. The description of the mission itself, however, provides encouraging motivation for our proposed demonstration of wavefront control with MEMS DMs and provides useful descriptions of preparatory analysis, tests, and on-orbit telemetry planning that we will incorporate into our CubeSat MEMS DM demonstration plan.

The James Webb Space Telescope microshutter array[41] is another example of a related impressive microarray designed and built for space operation with on/off functionality as a programmable mask whose development, integration, and test efforts can help inform the CubeSat DMD, but which still does not provide the needed high-accuracy demonstration of MEMS DM actuators on orbit over extended periods of time for the purpose of wavefront control.

1.6 Background on the CubeSat Platform

The CubeSat form factor was developed by California Polytechnic Institute (CalPoly) and Stanford University in 1999. It interfaces with a common secondary payload deployer, the Poly-picosatellite Orbital Deployer (P-POD), which significantly reduces the cost and time for obtaining launch opportunities for nanosatellites. The basic nanosatellite unit is a $10 \times 10 \times 10$-cm cube (called 1U). The P-POD unit will support a 3U volume in a variety of combinations.[42]

(a)   (b)   (c)
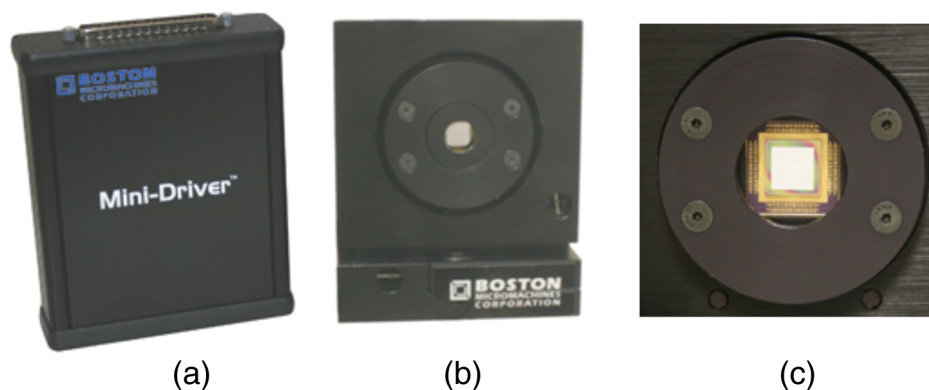
Fig. 2 Boston Micromachines Mini 6×6 (32 actuator) deformable mirror (DM) and drive electronics (Ref. 50). (a) Driver board packaging that would be removed; (b) mirror in packaging of which the exterior would be removed; and (c) close-up of the mirror. The drive electronics board could fit in a CubeSat without the packaging and with some minor modifications to the board.

For example, it can accommodate three 1U CubeSats, or, it can accommodate a single triple-long 3U CubeSat (which can be about 34.05-cm long instead of 30 cm, since space allocated for "feet" separating individual 1U CubeSats can be allocated to the volume of the single 3U). CubeSats are usually launched as secondary payloads on government or commercial primary missions, with their launch accommodation often sponsored by government agencies, such as the NASA Educational Launch of Nanosatellites program. A 3U CubeSat is an appropriate platform for the DM demonstration mission because it enables a comparatively quick, simple, low-cost approach for a technology demonstration whose results would have significant impacts on the design, scale, and capabilities of future space-based optical systems.

2 Payload for the CubeSat DM Demonstration Mission

The purpose of this section is to describe two concepts for a 3U CubeSat platform that demonstrate MEMS DM technology and increase the TRL of a miniaturized, low power, standalone wavefront control system for a space telescope: Payload concept 1 is a miniature Michelson interferometer and payload concept 2 is a Shack-Hartmann wavefront sensor.

Both of these concepts are in preliminary stages of development and will benefit from community input and laboratory demonstrations. The initial demonstration mission design is kept as simple as possible; in the future, additional CubeSats can be flown to perform demonstrations with increased complexity and functionality. The supporting spacecraft subsystems for the 3U CubeSat are described in greater detail in Sec. 3. For the purpose of evaluating payloads, we assume the following constraints on the payload mass (1.5 kg), volume (15 cm × 10 cm × 10 cm), power (5 W), and data rate (120 Mb/day). The remaining resources of the 3U CubeSat are required for communications, attitude control, power, command and data handling, and thermal subsystems.

2.1 Payload Requirements

While much work remains to be done to better define payload performance requirements, for the purpose of this feasibility evaluation, the payload shall be able to (1) demonstrate that high actuator count MEMS DMs can be commanded and controlled on-orbit for 1 month minimum with a 12 month goal; (2) use a simple static wavefront sensing system (such as interferometric, shear, or mask[43,44]) to characterize the performance of the MEMS mirror, including evaluation of individual actuator and multiple actuators contributing to mirror shapes such as tilt, Fourier, and Zernike modes (zonal and modal sensing[43]); and (3) demonstrate closed-loop control of mirror shape over integration times from 100 to 1000 s in the presence of thermal gradients and attitude control and structural jitter/instabilities.

It is important to keep in mind that this mission is to demonstrate functionality of an MEMS DM in a simple wavefront control system in orbit. It would add complexity and cost to levy exacting phase correction requirements on the system, although such an approach would be an appropriate advance in a follow-on mission.

2.2 Payload Design Trades

To meet the mission goals and keep costs low, the approach is to use as much existing commercial off the shelf (COTS) hardware as possible, making modifications as needed for operation in space, and to keep the design as simple as possible. We avoid mechanisms other than the DM itself to eliminate additional complexity and risk.

2.2.1 Internal or external light source

One major design trade is whether to use an internal light source (diode laser), an external (bright star) light sources, or both. The current mission objectives and payload requirements can be met using an internal laser as the light source. This would reduce cost and complexity since the ADCS would not need to maintain pointing at a star for long periods of time, which would require the use of a miniature CubeSat-sized reaction wheel assembly. The power requirement needed by a reaction wheel assembly is about 4 W. With an internal light source, the ADCS system could meet pointing requirements to Earth ground stations for communication downlink using only magnetic torque coils or rods. Use of an internal light source, such as a laser diode, would also be beneficial for routine calibration and monitoring of the system. The power requirement of the laser is <0.5 W for a 5-mW laser. A neutral density filter would also be needed to attenuate the laser signal so that it does not saturate the detector.

Having considered the benefits of using a diode laser as an internal light source, there is still the ultimate goal of using this technology on space telescopes that motivates the use of an external light source in demonstration, namely, a bright star. There are two operational approaches to imaging a star. One is to know what star we want to point at and navigating there, and this would require a CubeSat-sized star tracker along with the coarse (reaction wheels) and fine (steering mirror or device) attitude control actuators. Another approach is to image the stars but not to be particular about what is being imaged. Either way, imaging a star would drive the CubeSat system design in a way that would bring value to the future wavefront sensing space telescope missions, such as developing the ADCS algorithms that include both pointing and closed-loop wavefront control.

Due to the added complexity required of the ADCS system on a CubeSat platform, the external source imaging for this demonstration mission will not require a precise star acquisition and navigation system. Instead, with pointing knowledge from ADCS, the shutter on the aperture will be commanded to open when a bright star is in the field of view (FOV). Based on our preliminary models using STK looking at five bright stars (Alpha Centauri, Arcturis, Canopus, Sirius, and Vega), a satellite in the same orbit as the International Space Station (400 × 425 km and 51.6-deg inclination) would expect to see the same bright star every orbit for an average of 3–5 min. The pointing requirement on the maximum ADCS slew rate is then to keep the star on the same pixel on the detector for the duration of an exposure. To determine the pointing requirement that achieves this it is necessary to calculate the plate scale of the detector. The plate scale of the detector is the relationship between angular distance on the sky and pixel size on the detector, and is typically measured in arc sec /pixel. Using an estimated plate scale of 28 arc sec /pixel, the maximum

slew rate for ADCS during external source imaging can then be determined by dividing the plate scale by the maximum exposure time. Using a maximum exposure of 0.1 s, the maximum slew rate requirement during external source data acquisition is 4.7 arc min /s.

Our simulations have shown that active magnetic control using magnetorquers with magnetic moments of 0.65 Am^2 in each axis of a 3U CubeSat would be sufficient to counter environmental disturbances on orbit and achieve the slew rate requirement with pointing accuracy of between 1 and 10 deg and stabilization on the order of 0.12 deg.[45] While it may be interesting to include a miniature reaction wheel assembly in addition to magnetic torquers to assess the impact of reaction wheel disturbances on the wavefront control system, it does not appear necessary to enable imaging bright stars as targets of opportunity during an orbit. Estimates of pointing accuracy for a CubeSat sized reaction wheel assembly alone are 60 arc sec (3σ).[46,47] Additional work to evaluate the combined pointing accuracy needs of the optical system and capabilities of the CubeSat is needed for the proposed payload designs.

We plan to investigate, for a follow-on nanosatellite mission whose goal is to image specific stars, whether or not a fast steering (tip-tilt) mirror will be needed. It is generally accepted that a fast steering mirror will be needed on a larger space telescope. The fast steering mirror would allow for much more accurate pointing than a reaction wheel assembly can provide, and would also correct for tip and tilt errors in the wavefront that may be larger than the stroke of the DMs can correct for.

If an external light source looking at bright stars of opportunity is used, the aperture would necessarily be small given the CubeSat size constraints. As discussed in Sec. 3, not much space remains after accommodating the key elements of the system (DM, mirror drive electronics, imaging optics, and detector). Due to the need to accommodate a DM and reduce complexity, it is not practical to try to design a 3U CubeSat as a reflecting telescope using mirrors. While it may be possible to integrate a larger standard lens in the aperture (up to 75-mm diameter may be feasible in a 3U CubeSat), the corresponding longer focal length (>75.0 mm) is not an option due to the limited space available for all components and resizing the beam would be difficult. A smaller aperture and lens will limit the angular resolution ($1.22\lambda/D$) and sensitivity as well as increase the size of the PSF (which must also be Nyquist sampled by the pixels on the detector), but tight angular resolution is not a requirement for this technology demonstration. For a 1 in. (25.4 mm) or ½ in. lens (12.7 mm) diameter lens, which have minimum focal lengths on the order of their diameter, the angular resolution (width of the center of the point spread function) at 500 nm would be 1.2 arc sec (1 in.) and 2.4 arc sec (½ in.).

2.2.2 MEMS deformable mirrors

Even though MEMS DMs themselves are quite small, a widely acknowledged challenge to incorporating high actuator count DM systems on a spacecraft is the substantial size, mass, volume, power, and complexity of the mirror driver boards and wire harnesses.[34,38] While development of application-specific integrated circuit (ASIC) drivers is a current focus of several DM manufacturers,[48,49] it is uncertain when ASIC drivers will become generally available and whether

they will be appropriate for space applications. For the purpose of this technology demonstration, both the mirror and driver need to fit within the payload constraints as well as leave space for supporting optics and a detector. We are still investigating the ability of candidate mirror and driver systems from manufacturers such as Boston Micromachines Corporation (BMC, Cambridge, Massachusetts), Iris AO (Berkeley, California), and Xinetics (Devens, Massachusetts) to be redesigned for smaller-stroke applications such as this one to fit in drive electronics that could be easily accommodated in a CubeSat. We have currently identified and started laboratory experiments with a candidate DM, the 32-actuator "Mini" from Boston Micromachines, where both the DM and existing drive electronics board fit in the 1.5U payload volume of a 3U CubeSat without significant modification. We have also confirmed that with some minor modification to the drive electronics board, the Iris AO PTT111 (37 segment mirror) would fit as well. The baseline CubeSat DM payload design discussed here accommodates a BMC "Mini" DM from Boston Micromachines[50] with their new mirror housing design (dimensions roughly 50-mm diameter × 22.1-mm tall, note that the earlier model was 114.17 mm × 74.93 mm × 70.99 mm and would not fit[51]). The BMC Mini is a 6 × 6 DM (32 actuator, as the four corners are not active). There are three different stroke and aperture options with the Mini, as summarized in Table 1. There are trades to be further examined between stroke for nonatmospheric wavefront correction versus response time, pitch, and interactuator coupling. Having a larger stroke without increasing the number of possible voltage steps (bits in the digital to analog converter) also reduces the precision to which the actuators can be controlled.

The Mini DM has 14-bit step resolution and a subnanometer average step size. The fill factor is $>99\%$, the surface finish is <20 nm RMS, and the driver is completely powered and controlled by a USB 2.0 interface. The frame rate is 8 kHz, with a 34 kHz burst mode. As noted, the most recently available BMC Mini packaging format is selected (5-cm diameter and 2.21-cm tall, 75 g without cables). The existing Mini driver board has dimensions of $13 \times 10 \times 1.8$ cm currently. The initial plan is to use this board nearly as is with dimensions and layout slightly tweaked to fit in the CubeSat 10 cm × 10 cm form factor, making as few modifications as possible to the board and device (e.g., remove windows on the mirror before flight, replace electrolytic capacitors on the boards, apply conformal coating, and secure connectors).

Table 1 Boston Micromachines Mini MEMS deformable mirror options (Ref. 50).

Stroke	1.5 μm	3.5 μm	5.5 μm
Aperture	1.5 mm	2.0 mm	2.25 mm
Pitch	300 μm	400 μm	450 μm
Approx. mechanical response time (10%–90%)	20 μs	100 μs	500 μs
Approx. interactuator coupling ($\pm$5%)	15%	13%	22%

2.2.3 Wavefront sensors

There are many different approaches to wavefront sensing and reconstruction. To start with, there are both sensored and sensorless approaches, the former having the challenge of a noncommon optical path with the detector, and the latter requiring additional computational resources, time, and sometimes additional detectors or detector translation (such as Gerchberg-Saxton, phase diversity, or "lucky" imaging). For the exoplanet direct imaging application on a large space telescope mission, it is likely that a sensorless approach will be used to eliminate noncommon path optical errors. However, since the first goal in this work is mirror characterization and we do not expect to have a platform with the same stability and processing capability as a dedicated exoplanet direct imaging mission, in this work, we focus on two approaches to wavefront sensing selected from among several established methods[43] because they can be simply implemented in a compact form factor. We try to minimize the use of additional mechanisms such as rotating or translating components. Another important aspect to consider is the robustness of the sensor given the need to survive launch and function without intervention from on-orbit. The two approaches discussed in detail here are versions of (1) a Michelson interferometer and (2) a Shack-Hartmann wavefront sensor. There are additional wavefront sensing approaches that could be implemented, such as using an aperture mask to augment sensorless approaches, as well as improved or modified versions of the lenslet and shear sensing approaches that we investigate here, that we will consider in future work. One example of such an approach is a point diffraction interferometer,[52] which could be used in the place of a Michelson interferometer if the low light efficiency and decreased performance in conditions of high aberration are acceptable.

2.3 Concept 1: Michelson Interferometer

The Michelson interferometer concept is well known and has a variety of applications including wavefront sensing and surface characterization.[43,53] As shown in Fig. 3, collimated laser light reflects off both the DM and a flat mirror and is combined to form interference fringes on the detector. The laser light encounters a beam splitter (BS). The transmitted beam travels to the MEMS DM where it is reflected back to the BS. Half of this beam is deflected by 90 deg at the BS and strikes the detector. The other part of the beam travels to a flat mirror, where it is reflected back to the BS. Half of this light then passes straight through the BS and reaches the detector. The two beams that are directed toward the detector interfere to produce fringes that are analytically well understood as a function of beam coherence, divergence, and mirror angle (tip/tilt).[43,53,54] Fringe patterns can be simulated and demonstrated for a variety of other different mirror shapes and positions. The Michelson interferometer on a simple nanopositioning stage can be used for precise characterization of optical surfaces. The phase profile (and thus profile of optical path length) can be reconstructed by recording several images with different overall phase shifts. A phase-unwrapping algorithm can then be used to unambiguously retrieve surface maps extending over more than a wavelength. While not an issue for this application, very rough surfaces or very steep slopes may not be able to be successfully characterized with this method. The flat mirror is placed on

a linear nanopositioning stage to perform the phase adjustments for surface characterization using phase unwrapping. Figure 3 shows a notional placement of optical elements within the CubeSat constrained 95 mm × 150 mm area. The optical and optomechanical elements shown are baselined from Thorlabs (Newton, New Jersey), although more custom and robust mounting fixtures would be developed for the flight version. The detector is a UI-5241LE-M/C 1280 × 1024 pixel camera from Imaging Development Systems (Obersulm, Germany), and the DM is a 32-actuator Mini DM from Boston Micromachines. The nanopositioning stage shown is the P-753 LISA linear actuator and stage from Physik Instrumente (Karlsruhe/Palmbach, Germany). A CubeSat form-factor driver for the nanopositioning stage would also require some development and modification from the current version. Optical elements used in the payload would be selected and designed to survive the radiation environment, thermal environment, and launch and deployment shock and vibration, such as using UV-grade fused silica lenses with stress-free mounts in multipoint supported lens tubes. Several of these mounts would need to be custom made. The components will be housed within a black enclosure to eliminate stray light from the spacecraft bus.

Fringes from the interferometer can be generated both from a collimated source (straight fringes) or from a spherical point source that is diverging (radial fringes).[53] When the flatness or shape of a mirror changes, the resulting interference pattern is affected by changes as small as fractions of a wavelength. For basic piston and tip/tilt modes, it is straightforward to determine how well the DM is performing by studying the fringes in the images captured by the detector. For example, for a collimated beam, if the entire DM surface tilts by an angle θ from its original normal, the observed fringes occur at intervals of $\Delta x' = 2\lambda / \sin(\theta)$. If the DM surface moves forward (piston) by distance Δd, the observed fringe pattern moves as Δd changes, and the number of fringes that cross the center of the screen is $n = 2\Delta d/\lambda$.

Figure 4 shows the laboratory setup and initial tip-tilt results from a CubeSat-sized MEMS DM Michelson interferometer. The setup includes a 1.5 μm stroke Boston Micromachines Mini DM, a Thorlabs CPS180 635 nm 1 mW collimated laser diode module, a cube BS (which will distort less than the thinner BSs and has the added benefit of the coating being sealed inside the cube), a pinhole spatial filter, a neutral density filter, a flat mirror, and a Thorlabs DCC1545M ½ in. monochrome CMOS camera. A MATLAB interface to the mirror driver commands the 32 actuators into a "tilt" or "tip." Algorithms to analyze the images and fringe patterns compared with the DM commands are currently being tested.

2.4 Concept 2: Shack-Hartmann Wavefront Sensor

The Shack-Hartmann wavefront sensor is also well known in the field of adaptive optics and its basic concept appears to have predated even the Michelson interferometer.[55] The Shack-Hartmann sensor uses an array of lenslets across the pupil which all have the same focal length that are projected onto a detector. Each lenslet samples the local tilt of the wavefront, and this is evident in the position of that lenslet's focal spot on the detector. Any shape phase aberration of the whole wavefront is measured as a set of discrete tilts as measured by the lenslet array. Since only slopes are
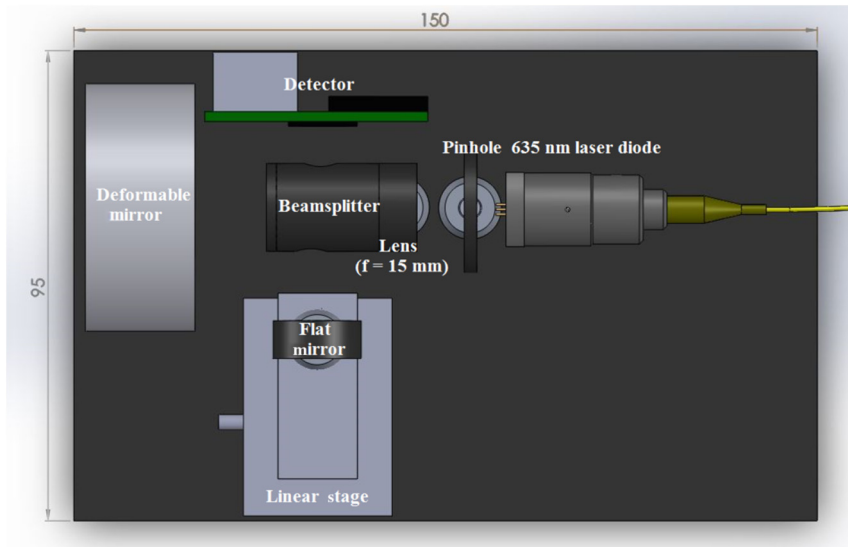
(a)
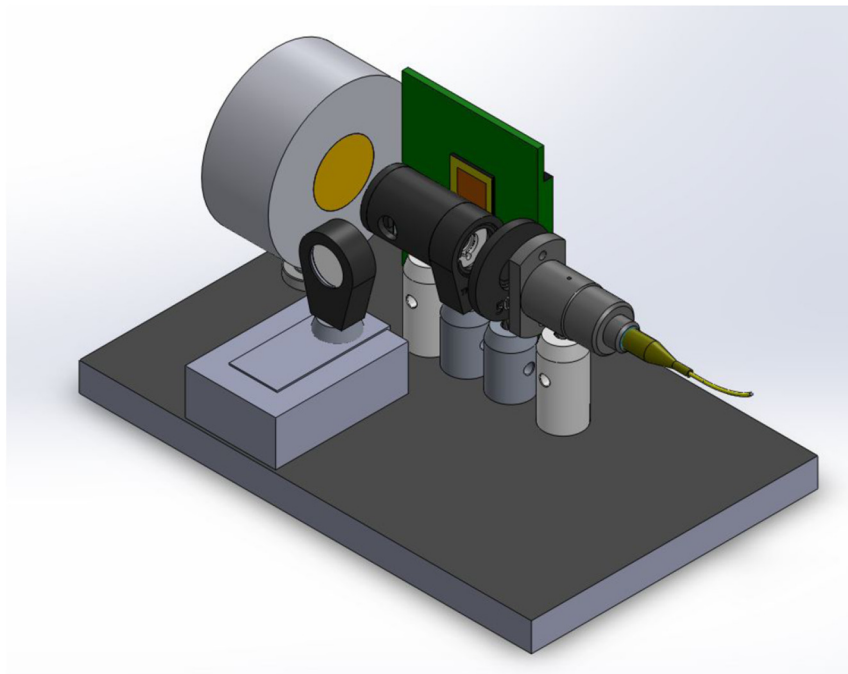
(b)

Fig. 3 (a) Top view of the Michelson interferometer payload that fits into a 95 mm × 150 mm footprint, which will fit in the 3U CubeSat payload volume. (b) Isometric view of the Michelson interferometer payload. A diode laser passes through a pinhole and is collimated before entering a 50/50 nonpolarizing beamsplitter. Light is reflected off both the flat mirror and the DM and is combined on the detector to form fringes.

measured, the Shack-Hartmann cannot detect discontinuous steps in the wavefront. Figure 5 shows a CubeSat Shack-Hartmann wavefront sensor payload. This design allows either a laser diode or an outside star or bright object to be used as the light source for the optical assembly. This light is linearly polarized and sent through a polarized beamsplitter. The polarized light reflects off the beamsplitter and passes through a quarter wave plate mounted between the beamsplitter and the DM. The beam that reflects off the DM passes through the quarter wave plate and is transmitted through the polarized beamsplitter, and through a series of lenses. A lenslet array is placed in front of the detector to

make a Shack-Hartmann sensor for this payload. Figure 5 shows a notional placement of optical elements within the CubeSat constrained 95 mm × 150 mm area. The optical and optomechanical elements shown are baselined from Thorlabs, although more custom, robust mounting fixtures would be developed for the flight version. The detector is a UI-5241LE-M/C 1280 × 1024 pixel camera from Imaging Development Systems, and the DM is a 32-actuator Mini DM from Boston Micromachines.

Figure 5 shows renderings of a CubeSat MEMS DM payload using a Shack-Hartmann wavefront sensor with both an internal laser diode light source as well as a path for looking
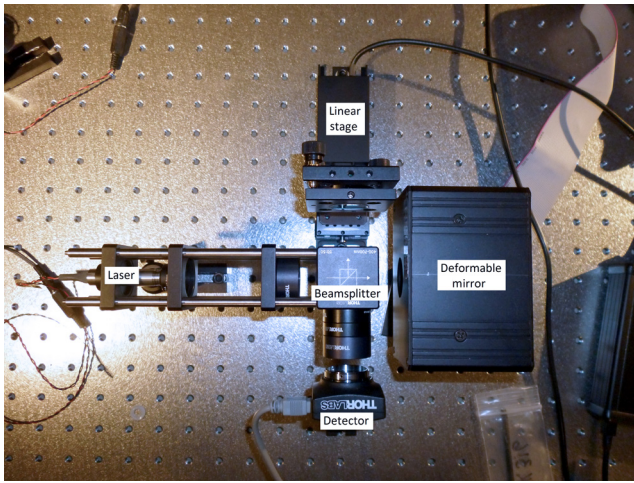
Fig. 4 CubeSat-sized MEMS DM Michelson interferometer prototype experiment. The setup includes a 1.5 μm stroke Boston Micromachines Mini DM, a Thorlabs CPS180 635 nm 1 mW round beam collimated laser diode module, a cube beam splitter, a pinhole spatial filter, a neutral density filter, a flat mirror, and a Thorlabs DCC1545M ½ in. monochrome CMOS camera. A MATLAB interface to the mirror driver is commanding the 32 actuators into a "tilt" or "tip."

at stellar objects through an aperture. Operationally, the characterization of the mirror using the internal light source could be done first using the laser diode, and then once the primary mission goals are satisfied, the laser could be turned off and objects from the aperture could be observed. The laser would be coherent and orders of magnitude brighter than any star in the aperture.

Figure 6 shows the intensity measurement and Michelson interferometer fringes observed when the MEMS DM is commanded to perform an effective tilt. The percent tilt is in terms of the maximum displacement of the actuator. A tilt of 33% means that the actuators on the furthest side of the tilt are at 33% of their maximum allowed displacement. Software to analyze the fringe patterns and infer mirror commands from observations is currently under development.

In Fig. 7, individual actuators were commanded to their maximum allowed displacement level. Different shapes were commanded to the mirror in Fig. 8, namely three different Zernike polynomials. Given the square aperture and organization of the actuators for the BMC Mini DM, it would probably be best to use Fourier modes for characterization of the mirror in future work.

The initial results shown in Figs. 6–8 show that different types of commands to the MEMS DM can be captured and are fairly easily distinguishable from each other by either a Shack-Hartmann wavefront sensor or Michelson interferometer, although much work remains in order to quantify the response of the mirror to commands as detected by the sensing system.

2.4.1 Mission concept of operations

The use of an internal light source for the initial demonstration of DM functionality in-orbit eliminates any payload-specific requirements on the CubeSat's altitude and inclination. The orbit altitude range of 400 to 600 km is limited on the upper constraint by the CubeSat maximum

de-orbit time requirement and on the lower constraint by drag and the desired mission lifetime of 1 year. A high-level overview of the concept of operations includes phases for launch, deployment, and detumbling, 30 days of commissioning, and a success threshold of 1 month of nominal operations and data downlink with a goal of 12 months of nominal operations and data downlink. The first phase of nominal operations involves open-loop wavefront sensing of a repeating sequence of mirror surface shapes during which characterization and calibration is performed. This is followed by the second phase of the mission, closed-loop wavefront sensing, where the CubeSat microcontroller is used to achieve and maintain a desired surface shape on the DM. This is followed by a third phase, whose purpose is to simulate the effects of bad actuators and increasingly noisy signals before de-orbiting.

3 CubeSat Subsystems

3.1 Power

Two solar panel configurations were modeled in STK: (1) a set of four 3U body-mounted panels, shown in Fig. 9 and (2) a set of four two-sided 3U deployed solar panels and no body-mounted panels. Each 3U surface holds seven ultra-triple junction solar cells. In each case, the spacecraft is oriented with the long axis parallel to the zenith-nadir line. The results from power generation calculations for a series of orbital altitudes and inclinations for each configuration for one orbit are shown in Table 2, which compares the orbit-averaged power (averaged over daylight, nonzero power generation) for each case. Simulations show that although the peak power generation is generally higher with the deployed panels, the body-mounted panels provide more uniform power generation across the orbit.

Although the peak power generation is higher with the deployed solar panel configuration, a calculation of the orbit-averaged power shows that the body-mounted panel generation is more favorable than that of the deployed panels for missions where the body-mounted solar panels will not be obstructed, for example, due to the presence of an antenna, sensor, or instrument FOV. Using only deployed panels does not provide a significant increase in power generation; it makes for a less consistent power profile, and deployed panels add unnecessary complexity and cost to the spacecraft. For these reasons, the current design utilizes four 3U body-mounted panels.

If further analysis shows that more power generation is required, additional options can be considered. One is to utilize deployed panels in conjunction with body-mounted panels. Another is to design the spacecraft to enable solar array sun tracking, which would require a more robust ADCS design, articulated solar panels, or both.

3.2 Structure

The basic structure of the spacecraft is a 3U CubeSat with body-mounted solar panels. Figure 9 shows the outer chassis structure of the 3U CubeSat with volume-representative subsystems and components, as detailed in Fig. 10.

A preliminary placement of the subsystem boards and payloads within the 3U CubeSat volume is shown in Fig. 10. To enable image processing capability onboard, a flight computer like the Clyde Space FPGA-based Mission
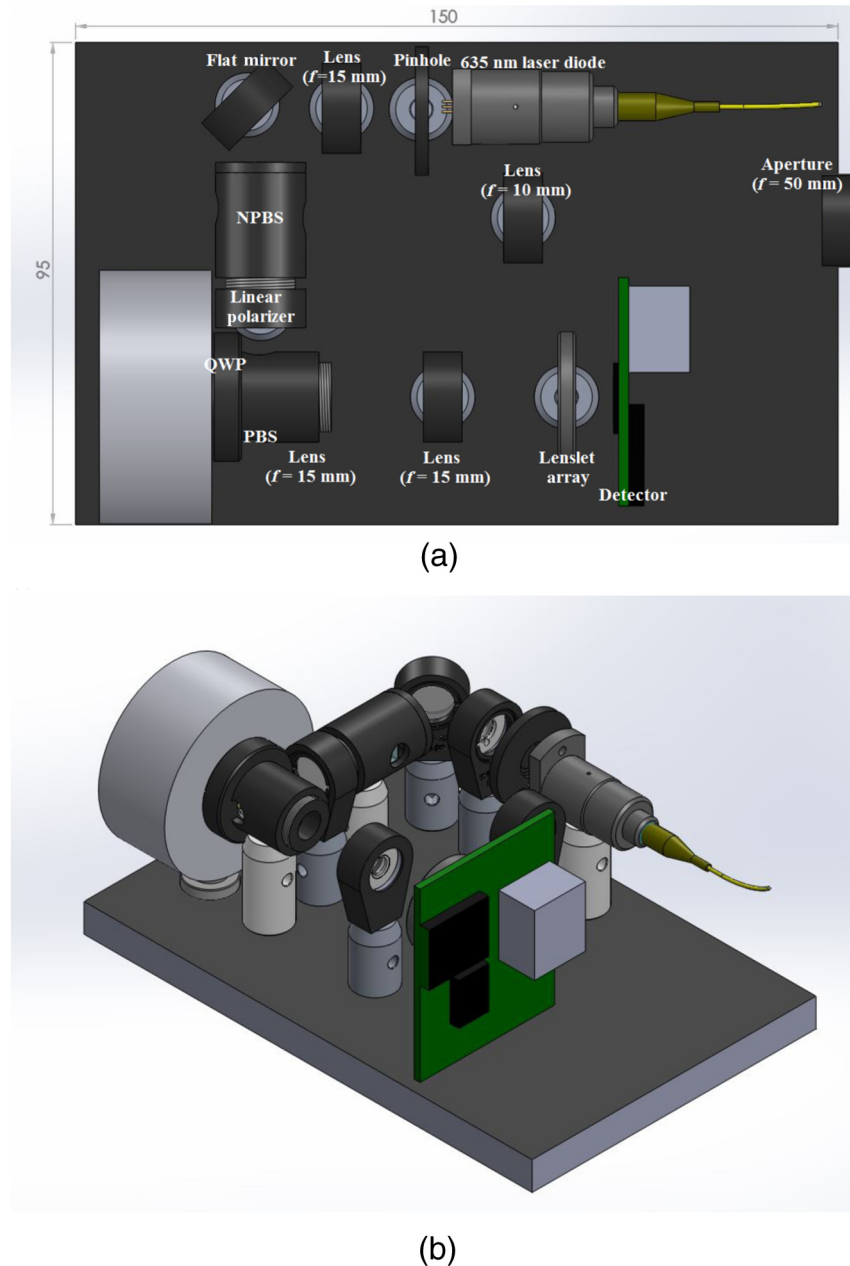
Fig. 5 (a) Top view of the Shack-Hartmann wavefront sensor payload that fits into a 95 mm × 150 mm footprint, which will fit, with supporting subsystems, in the 3U CubeSat payload volume. (b) Isometric view of the Shack-Hartmann wavefront sensor payload. The laser diode generates light that passes through a pinhole, gets collimated by the lens, reflects off the flat mirror, and transmits through the first (nonpolarizing) beamsplitter before entering the linear polarizer. A half-inch aperture lens admits light from an outside source that is collimated and reflects off the nonpolarizing beamsplitter before entering the linear polarizer. A lenslet array is used to image the pupil plane onto the detector. The diode laser can be turned on to dominate the system at any time.

Interface Computer would be used. The electrical power system modeled here is from Clyde Space, and the structure is a Pumpkin 3U skeletonized chassis. The communications system is a UHF Cadet nanosatellite radio from L-3 Communication Systems West. The payload takes up a volume of approximately 1.5U.

3.3 Attitude Determination and Control System

The ADCS for the internal light source design (with imaging of external target stars of opportunity) needs only to achieve pointing toward a ground station for communication and to keep the spacecraft from slewing at rates above about 4.7 arc min /s. The payload is housed entirely within the bus structure and its operability is not affected by the attitude or orientation of the spacecraft (although sensitivity to disturbances is another area under study). Although passive magnetic control is a simple approach that has flown on previous CubeSat missions,[56] our simulations show that to allow imaging bright stars through an aperture would require active magnetic control to counter environmental disturbances. Torque coils with magnetic moments of about 0.65 Am^2 per axis for a 3U CubeSat would be able to meet this requirement.
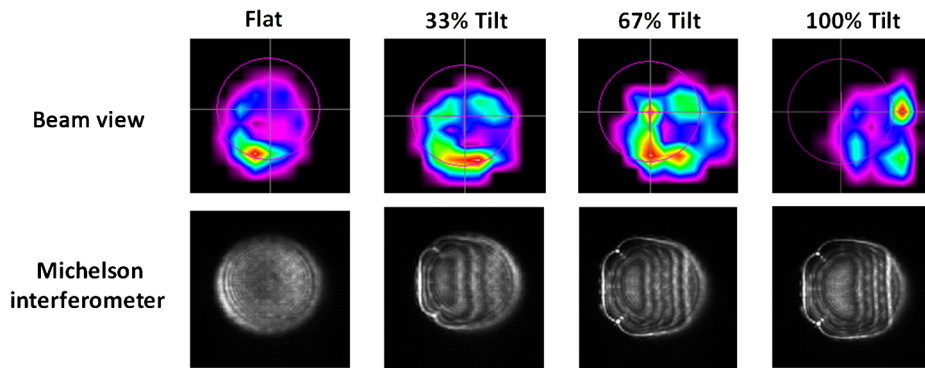
Fig. 6 Example results looking at different steepness tilts on the MEMS DM the Michelson interferometer prototype (Michelson without nanopositioning stage here). The "beam view" is the laser intensity as reflected off of the MEMS DM.
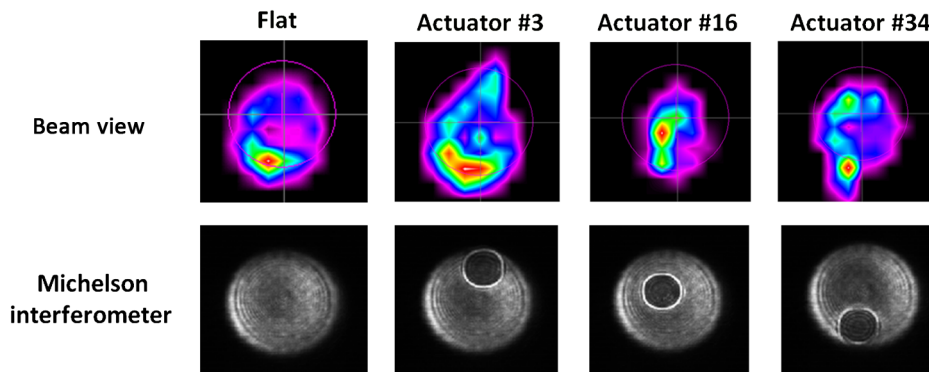
Fig. 7 Example results looking at different actuator "pokes" on the MEMS DM. The "beam view" is the laser intensity as reflected off of the MEMS DM.
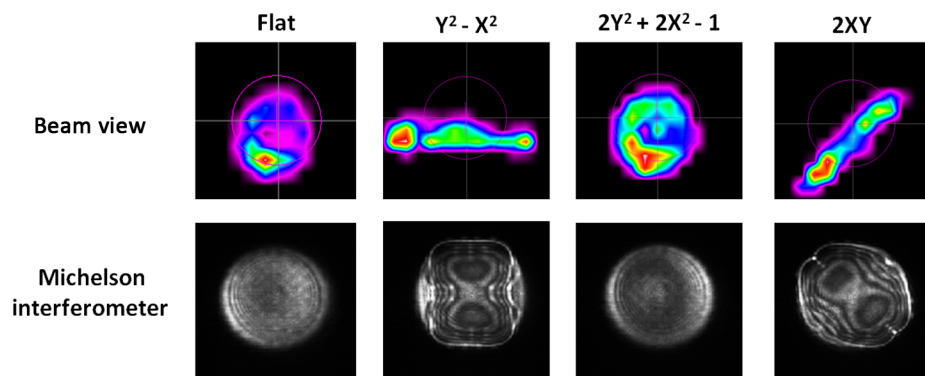
Fig. 8 Example results looking at different Zernike polynomials on the MEMS DM. The "beam view" is the laser intensity as reflected off of the MEMS DM.

A sensor package of a magnetometer, IMU, and coarse sun sensors would satisfy the relatively flexible pointing requirements of this mission (1 to 10 deg, depending on the inclination and variability of the magnetic field).

Pointing the CubeSat at a particular target star and maintaining lock on that star for an observation would require a substantial amount of additional cost and complexity to the mission. Currently available reaction wheel assemblies with CMOS or infrared (thermopile) Earth horizon sensors are not anticipated to achieve better than 0.5 deg of pointing knowledge. A star tracker and multistage control system could improve this to possibly as good as 1 arc min, however, COTS CubeSat reaction wheel assemblies with star trackers are not yet available (and are anticipated to be at a higher price point than existing reaction wheel assemblies).

3.4 Thermal

The baseline thermal design is a passive system with the exception of the Clyde Space battery, which includes internal heaters. A comprehensive thermal model of the satellite and a more in-depth analysis of the payload components will

(a)   (b)
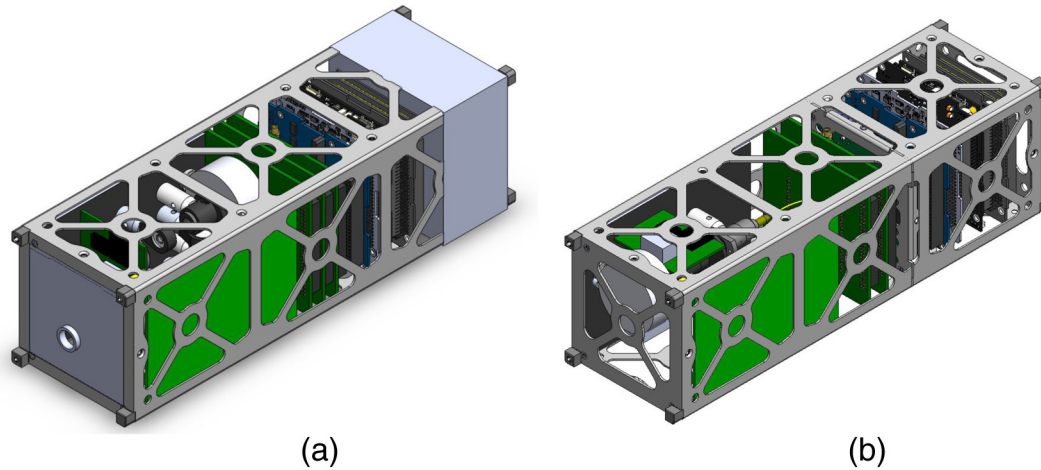
Fig. 9 (a) Isometric view of the Shack-Hartmann CubeSat with MEMS DM. (b) Isometric view of the Michelson interferometer CubeSat with MEMS DM and nanopositioning stage. Each of the payloads fit in the 1.5U payload volume allocated to them (a 95 mm × 150 mm footprint, which will fit in the 3U CubeSat payload volume). All components will be housed inside a 3U CubeSat with body-mounted solar panels covering the outer walls. Antennas for communication would be mounted on the sides or nadir face of the structure, which would be maintained in a gravity gradient orientation (with the aperture zenith pointing).

determine the need for active thermal management. Small flexible heater circuits, such as those from Minco (Minneapolis, Minnesota), may be required for spot thermal management, such as near the Thorlabs CPS405 laser diode (however, the CPS405 is engineered to survive −40 to 80°C and operate in −10 to 40°C).

3.5 Communications

The communications system will consist of a Cadet nano-satellite UHF radio from Level 3 Communications West. The UHF radio board is half-duplex and will use radio frequencies in the 445 to 455 MHz (uplink) and 460 to 470 MHz downlink. Ground stations such as the 18-m

dish at NASA Wallops would enable a robust communications link and a sufficient rate of data downlink.

3.6 Payload Components

Examples of some COTS payload components include a collimated laser diode such as the CPS405 from Thorlabs, a 4.5 mW, 405-nm laser which takes 5 volts direct current (VDC) regulated power and has a −10 to 40°C operating temperature range. Fused silica optics are commercially available that would satisfy the payload requirements. The BMC 6 × 6 (32 actuator) Mini DM options are summarized in Table 1, and only minor modifications to the driver board would be required. One possible option for a detector is a UI-5241LE-M/C 1280 × 1024 pixel camera from Imaging Development Systems.
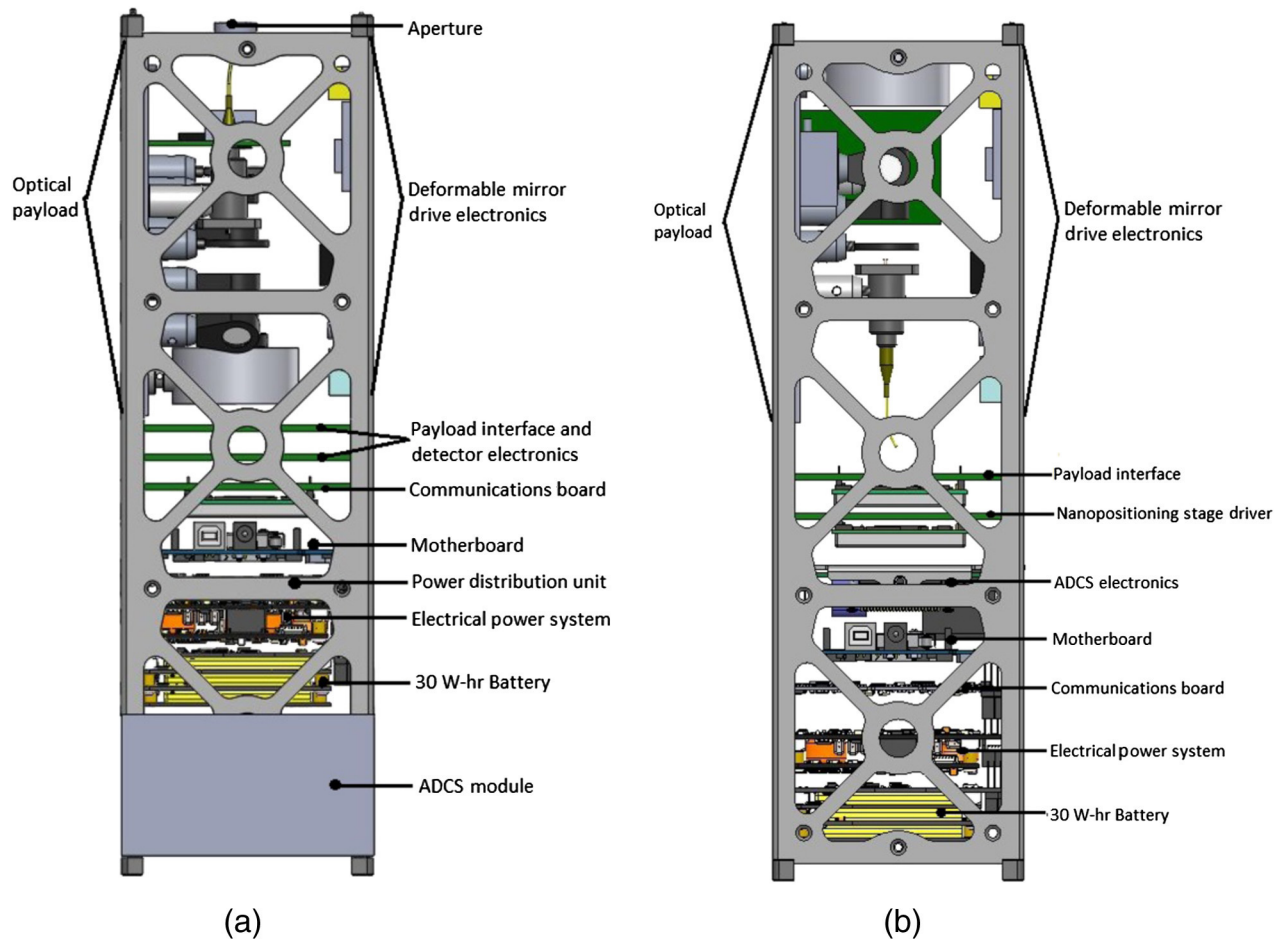
4 Summary and Future Work

4.1 Summary

Direct imaging of an Earth-like exoplanet requires an imaging system capable of achieving contrasts of 1×10^{-10}. Such contrast can be obtained through the use of active optics systems operated on space telescopes. High actuator count DMs are a key technology for this application, but their TRL must be increased before they can be viably incorporated into such missions. In this paper, we have shown that it is feasible to design a 3U CubeSat platform that can accommodate an MEMS DM demonstration experiment using COTS and CubeSat parts and components. Hardware laboratory bench tests of both the Shack-Hartmann and Michelson interferometer payload options are in progress. Each option offers a simple payload architecture that would enable characterization of the in-orbit performance of the DM. The Shack-Hartmann payload design may be easier to use for wavefront reconstruction and, additionally, provides the opportunity to detect stars as well as to use an internal light source for calibration and characterization.

Table 2 Orbit average generated power.

Orbital inclination (deg)	Orbital altitude (km)	4 × 3U body-mounted panels orbit avg. generated power (W)	4 × two-sided 3U deployed panels orbit avg. generated power (W)
0	300	12.3	12.0
0	400	12.4	11.9
0	500	12.2	11.8
45	300	11.9	12.1
45	400	12.2	12.1
45	500	12.2	12.1
90	300	14.8	6.2
90	400	15.0	6.4
90	500	15.0	6.4

Fig. 10 Subsystems stack and payload accommodation in the 3U CubeSat for (a) the Shack-Hartmann CubeSat with MEMS DM and (b) the Michelson interferometer CubeSat with MEMS DM and nanopositioning stage. Each of the payloads fit in the 1.5U payload volume allocated to them (a 95 mm × 150 mm footprint, which will fit in the 3U CubeSat payload volume).

4.2 *Future Work: Follow-on Missions*

There are several different follow-on opportunities that could be pursued as a result of this simple DM demonstration. One of the more interesting options would be to use the same platform for a different small DM and driver for comparison. Next steps would involve incorporating a compact external-viewing camera system that is imaging (and tracking) an astronomical object. The long-term goal is to enable the use of small DMs for space imaging and free space communication applications on any size payload and spacecraft.

References

1. A. Wolszczan and D. Frail, "A planetary system around the millisecond pulsar PSR1257 + 12," *Nature* **355**(6356), 145–147 (1992).
2. M. Mayor and D. Queloz, "A Jupiter-mass companion to a solar-type star," *Nature* **378**, 355–359 (1995).
3. N. J. Kasdin et al., "Extrasolar planet finding via optimized apodized pupil and shaped pupil coronagraphs," *Astrophys. J.* **582**, 1147–1167 (2003).
4. X. Bonfils et al., "The HARPS search for southern extra-solar planets VI: a Neptune-mass planet around the nearby M dwarf Gl 581," *Astron. Astrophys. Lett.* **443**(3), L15–L18 (2005).
5. W. Borucki et al., "Kepler-22b: a 2.4 Earth radius planet in the habitable zone of a sun-like star," *Astrophys. J.* **745**(2), 120–136 (2012).
6. M. Tuomi et al., "Signals embedded in the radial velocity noise. Periodic variations in the tau Ceti velocities," *Astron. Astrophys.* **551**(A79), 21 (2012).
7. E. Palle et al., "Earth's transmission spectrum from lunar eclipse observations," *Nature* **459**(7248), 814–816 (2009).
8. T. Evans et al., "The deep blue color of HD 189733b: albedo measurements with HST/STIS at visible wavelengths," *Astrophys. J. Lett.* **772**(2), L16 (2013).
9. D. Charbonneau et al., "Detection of an extrasolar planet atmosphere," *Astrophys. J.* **568**(1), 377–384 (2002).
10. B. O. Demory et al., "Inference of inhomogeneous clouds in an exoplanet atmosphere," in press (2013).
11. M. Webber et al., "Effect of clouds on exoplanet transit, secondary eclipses, and phase curve observations," in *10th Annual Astrobiology Graduate Conf., Poster Session 1*, Montreal (2013).
12. M. S. Marley et al., in Protostars and Planets V, B. Reipurth, D. Jewitt, and K. Keil, Eds., Atmospheres of Extrasolar Giant Planets, pp. 733–474 University Arizona Press, Tucson, Arizona (2007).
13. J. J. Fortney et al., "A unified theory for the atmospheres of the hot and very hot Jupiters: two classes of irradiated atmospheres," *Astrophys. J.* **678**(2), 1419–1435 (2008).

14. E. Miller-Ricci, D. Sasselov, and S. Seager, "The atmospheric signatures of super Earths: how to distinguish between hydrogen-rich and hydrogen-poor atmospheres," *Astrophys. J.* **690**, 1056–1067 (2009).
15. L. Kaltenegger, W. Traub, and K. Jucks, "Spectral evolution of an Earth-like planet," *Astrophys. J.* **658**(1), 598–616 (2007).
16. K. Cahoy et al., "Exoplanet albedo spectra and colors as a function of orbital phase, separation, and metallicity," *Astrophys. J.* **724**(1), 189–214 (2010).
17. A.-L. Maire et al., "Atmospheric characterization of cold exoplanets using a 1.5-m coronagraphic space telescope," *Astron. Astrophys.* **541**(A83) (2012).
18. B. Benneke and S. Seager, "Atmospheric retrieval for super-earths: uniquely constraining the atmospheric composition with transmission spectroscopy," *Astrophys. J.* **753**(2), 100 2012).
19. R. Hu, B. Ehlmann, and S. Seager, "Theoretical spectra of terrestrial exoplanet surfaces," *Astrophys. J.* **752**(1), 900–908 (2012).
20. M. Kuchner and W. Traub, "A coronagraph with a band-limited mask for finding terrestrial planets," *Astrophys. J.* **570**, 200.
21. O. Guyon et al., "Exoplanet imaging with a phase-induced amplitude apodization coronagraph. I. Principle," *Astrophys. J.* **622**, 744–758 (2005).
22. E. Serabyn, D. Mawet, and R. Burruss, "An image of an exoplanet separated by two diffraction beamwidths from a star," *Nature* **464**(7291), 1018–1020 (2010).
23. D. Mawet et al., "The vector vortex coronagraph: laboratory results and first light at palomar observatory," *Astrophys. J.* **709**(1), 53–57 (2010).
24. P. Deroo, M. Swain, and R. Green, "Spectroscopy of exoplanet atmospheres with the FINESSE Explorer mission," *Proc. SPIE* **8442**, 844241 (2012).
25. W. Cash et al., "External occulters for direct observation of exoplanets: an overview," *Proc. SPIE* **6687**, 668712 (2007).
26. R. G. Lyon et al., "Visible nulling coronagraphy for exo-planetary detection and characterization," in *Direct Imaging of Exoplanets: Science & Techniques*, Vol. 200, pp. 345–352, Cambridge (2006).
27. D. Defrere et al., "Direct imaging of exoEarths embedded in clumpy debris disks," *Proc. SPIE* **8442**, 84420M (2012).
28. V. V. Sobolev, *Light Scattering in Planetary Atmospheres*, Vol. 76, International Series of Monographs in Natural Philosophy, Elsevier (1975).
29. B. R. Oppenheimer and S. Hinkley, "High-contrast observations in optical and infrared astronomy," *Annu. Rev. Astron. Astrophys.* **47**(1), 253–289 (2009).
30. K. Stapelfeldt, "Extrasolar planets and star formation: science opportunities for future ELTs," in *The Scientific Requirements for Extremely Large Telescopes, Proc. of the 232nd Symposium of the Int. Astronomical Union*, P. Whitelock, M. Dennefeld, and B. Leibundgut, Eds., pp. 149–158 (2005).
31. C. Correia et al., "On the optimal reconstruction and control of adaptive optics systems with mirror dynamics," *J. Opt. Soc. Am. A* **27**(2), 333–349 (2010).
32. R. Angel, "Ground based imaging of extrasolar planets using adaptive optics," *Nature* **368**, 203–207 (1994).
33. A. Sivaramakrishnan et al., "Speckle decorrelation and dynamic range in speckle noise limited ranging," *Astrophys. J.* **581**, L59 (2002).
34. M. Perrin et al., "The structure of high strehl ratio point-spread functions," *Astrophys. J.* **596**, 702 (2003).
35. B. Macintosh et al., "The Gemini Planet Imager: from science design to construction," *Proc. SPIE* **7015**, 701518 (2008).
36. O. Guyon, T. Matsuo, and R. Angel, "Coronagraphic low-order wavefront sensor: principle and application to a phase-induced amplitude apodization coronagraph," *Astrophys. J.* **693**, 75–84 (2009).
37. National Research Council, New Worlds, New Horizons in Astronomy and Astrophysics, http://www.nap.edu/catalog.php?record_id=12951 (2010).
38. C. Mendillo et al., "Flight demonstration of a milliarcsecond optical pointing system for direct exoplanet imaging," *Applied Optics* **51**(29), 7069–7079 (2009).
39. J. Lee et al., "A new type of space telescope for observation of extreme lightning phenomena in the upper atmosphere," *IEEE Trans. Geosci. Remote Sens.* **50**(10), 3941–3949 (2012).
40. B. Yoo et al., "MEMS micromirror characterization in space environments," *Opt. Express* **17**(5), 3370–3380 (2009).
41. A. Kutyrev et al., "Programmable microshutter arrays for the JWST NIRSpec: optical performance," *IEEE J. Sel. Top. Quantum Electron.* **10**(3), 652–661 (2004).
42. J. Puig-Suari, C. Turner, and R. Twiggs, "CubeSat: the development and launch support infrastructure for eighteen different satellite customers on one launch," in *Small Satellite*, pp. SSC01-VIIIb-5 (2001).
43. R. K. Tyson, *Principles of Adaptive Optics*, CRC Press, Boca Raton, Florida (2011).
44. F. Martinache, "The asymmetric pupil Fourier wavefront sensor," *Proc. Astron. Soc. Pacific* submitted for publication (2013).
45. S. Gregory, *Attitude Control System Design for ION, the Illinois Observing Satellite*, University of Illinois, Urbana (2004).
46. M. W. Smith et al., "ExoplanetSat: detecting transiting exoplanets using a low-cost CubeSat platform," *Proc. SPIE* **7731**, 773127 (2010).
47. C. Pong et al., "Achieving high-precision pointing on ExoplanetSat: initial feasibility analysis," *Proc. SPIE* **7731**, 7731V (2010).
48. X. Wu, L. Yao, and H. Ou, "Novel hierarchically dimensioned deformable mirrors with integrated ASIC driver electronics," *Proc. SPIE* **8253**, 82530A (2012).
49. J. Stewart, "Compact low power driver for deformable mirror systems," (2009).
50. Boston Micromachines Corporation, Deformable Mirrors (2011).
51. Thorlabs Inc., Thorlabs Adaptive Optics Kits. http://thorlabs.com/thorcat/18100/DM32-35-UM01-AutoCADPDF.pdf (July 2013).
52. R. N. Smartt and W. H. Steel, "Theory and application of point diffraction interferometers," *Jpn. J. Appl. Phys.* **14**, 351–356 (1974).
53. F. Traeger, *Springer Handbook of Lasers and Optics*, Springer, New York (2007).
54. W. Demtroeder, *Laser Spectroscopy, Basic Concepts and Instrumentation*, 3rd ed., Springer-Verlag, Berlin (2003).
55. C. Scheiner, "Oculus, sive fundamentum opticum," (1619).
56. J. Springmann et al., "The attitude determination system of the RAX satellite," *Acta Astron.* **75**, 120–135 (2012).

Kerri L. Cahoy received a BS (2000) in electrical engineering from Cornell University, and an MS (2002) and PhD (2008) in electrical engineering from Stanford University. After working as a senior payload engineer at Space Systems Loral, she was an NASA postdoctoral program fellow at NASA Ames Research Center and a research scientist at Massachusetts Institute of Technology (MIT)/NASA Goddard Space Flight Center. She is currently a Boeing assistant professor in the MIT, Department of Aeronautics and Astronautics.

Anne D. Marinan earned her BS in aerospace engineering from the University of Michigan, Ann Arbor, in 2011. She is a second-year master's candidate at the MIT in the Space Systems Laboratory and associated Wavefront Control Laboratory. Her research interests include systems level analysis of designing constellations of CubeSats and applying adaptive optics to space-based applications.

Benjamin Novak will receive a BS in aeronautics and astronautics from MIT in 2015. He is also pursuing minors in economics and astronomy. He worked in several laboratories while at MIT, including the Wavefront Control Laboratory, on topics ranging from wavefront control systems to long endurance UAV missions.

Caitlin Kerr will receive a BS in aerospace engineering from MIT in 2015. She currently works as an undergraduate researcher in MIT's Wavefront Control Laboratory as part of the Star–Planet Simulator Team. Her areas of interest include high contrast imaging, the design, implementation, and operation of space systems, and engineering management and leadership.

Tam Nguyen received a BS in physics and in engineering as recommended by the Department of Aeronautics and Astronautics from MIT in 2013. She is currently a first-year graduate student in the Space Systems Laboratory at MIT, pursuing a master's degree in aeronautics and astronautics.

Matthew Webber received a BS in physics and mathematics from Northeastern University in 2012 while doing research at Draper Laboratory and the Harvard-Smithsonian Center for Astrophysics. He is currently pursuing a PhD at MIT in planetary science, researching exoplanet detection, astrophysics, and astrobiology.

Grant Falkenburg will receive a BS in electrical engineering from the MIT in 2016. He worked as an undergraduate researcher in MIT's Wavefront Control Laboratory.

Andrew Barg will graduate from Choate Rosemary Hall in 2014. He worked as a researcher in MIT's Wavefront Control Laboratory for the summer of 2013.